

pubs.acs.org/JPCL Letter

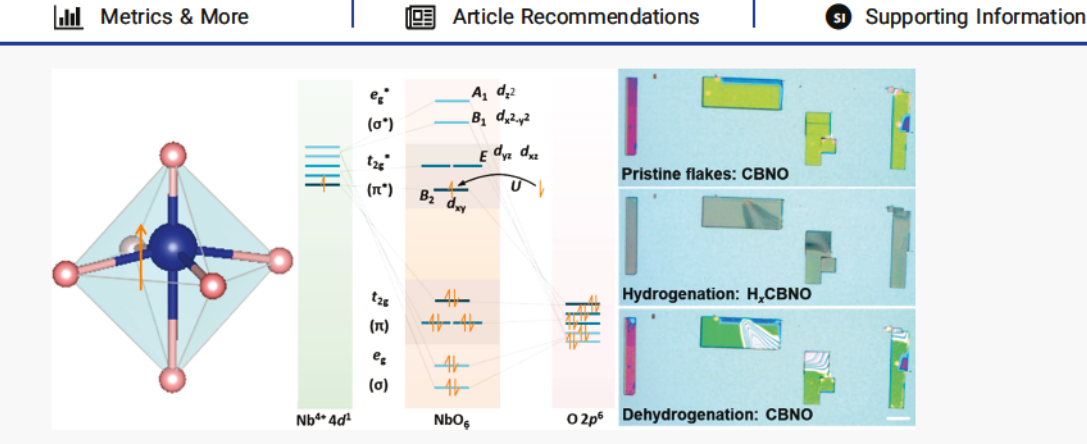
# Doping-Enabled Reconfigurable Strongly Correlated Phase in a Quasi-2D Perovskite

Lifu Zhang,<sup>†</sup> Jie Jiang,<sup>†</sup> Yao Cai, Shukai Yao, Bilal Azhar, Zhizhong Chen, Yang Hu, Saloni Pendse, Yuwei Guo, Ru Jia, Zhiting Tian, Chengliang Sun, Peilin Liao, and Jian Shi\*



**ACCESS** I





ABSTRACT: Highlighted by the discovery of high-temperature superconductivity, strongly correlated oxides with highly distorted perovskite structures serve as intriguing model systems for pursuing emerging materials physics and testing technological concepts. While 3d correlated oxides with a distorted perovskite structure are not uncommon, their 4d counterparts are unfortunately rare. In this work, we report the tuning of the electrical and optical properties of a quasi-2D perovskite niobate CsBiNb<sub>2</sub>O<sub>7</sub> via hydrogenation. It is observed that hydrogenation induces drastic changes of lattice dynamics, optical transmission, and conductance. It is suggested that changing the orbital occupancy of Nb d orbitals could trigger the on-site Coulomb interaction in the NbO<sub>6</sub> octahedron. The observed hydrogen doping-induced electrical plasticity is implemented for simulating neural synaptic activity. Our finding sheds light on the role of hydrogen in 4d transition metal oxides and suggests a new avenue for the design and development of novel electronic phases.

oping (including both chemical and electrostatic doping) has served as a common mechanism for a plethora of applications,  $^{1-4}$  ranging from superconductors to artificial intelligence.  $^{5-8}$  Doping-driven phase transition and doping tuning of physical properties are particularly common in correlated perovskite oxides with d-electrons.  $^{9-14}$  Typical manifestations of doping tuning of physical properties in correlated materials include high  $T_{\rm C}$  superconductivity,  $^{15}$  colossal magnetoresistance,  $^{16}$  and multiferroicity.  $^{17}$ 

In this Letter, we explore the role of hydrogen doping on niobate with a quasi-2D Dion–Jacobson oxide CsBiNb<sub>2</sub>O<sub>7</sub> (CBNO) as the model material. It is shown that hydrogenation of the pristine CBNO (Nb<sup>5+</sup> is reduced to Nb<sup>4+</sup> having a 4d<sup>1</sup> electronic state) leads to pronounced change of optical and electrical properties, lattice dynamics, and electronic band structure. Inspired by the observed plasticity, we propose a novel neural network based on proton synaptic transistors with H<sub>x</sub>CBNO as the channel material.

Hydrogenation was adopted as the technique to reconfigure the electronic structure of our model material, CBNO. The small radius and midrange electronegativity of a hydrogen atom result in fast diffusion kinetics making hydrogenation an effective technique to tune the electron filling configuration. Successful examples of hydrogenation to enable new correlated phases or tune physical properties include hydrogenation of vanadium oxide, rare earth nickelates, 13,23–25 and superconducting copper oxides.

CBNO single crystals were first prepared via a molten-salt approach<sup>28</sup> (more details are presented in Methods). A representative crystal approximately one centimeter in size is shown in the top-left panel of Figure 1a. The as-grown crystals were exfoliated into flakes and transferred on a Si(100) substrate, as shown in the optical image in the uppermost right panel of Figure 1a. CBNO flakes have a lateral size of 20–100

Received: January 31, 2021 Accepted: May 19, 2021 Published: May 24, 2021





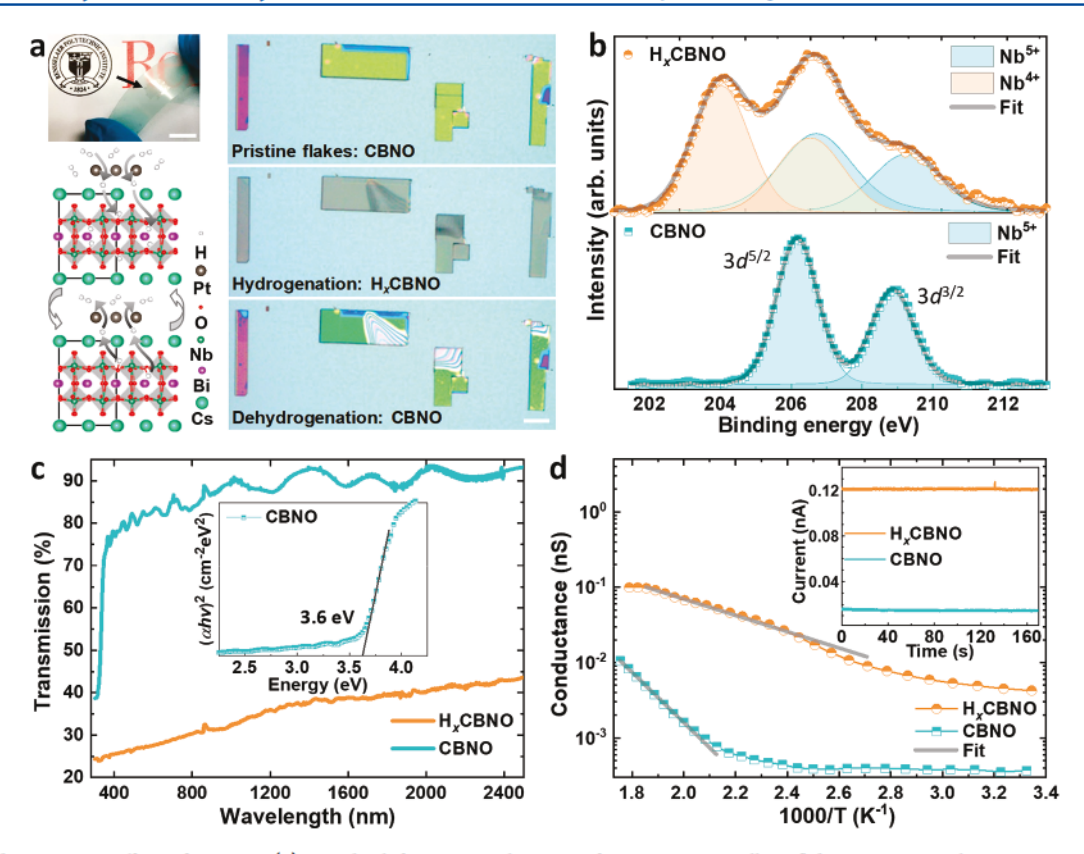


Figure 1. Hydrogenation effect of CBNO. (a) On the left, an optical image of a CBNO crystalline flake approximately 1 cm  $\times$  1 cm in size on a bent thermal release tape (top-left panel) and schematic of the hydrogenation and dehydrogenation process (bottom-left panel); on the right, optical images of flakes before (top-right panel, CBNO) and after hydrogenation (middle-right panel, H<sub>x</sub>CBNO) and dehydrogenation (bottom-right panel, CBNO) on Si(100) substrate. Scale bar: 1 cm for top-left panel and 25  $\mu$ m for right panels. (b) XPS spectra of Nb 3d in CBNO (bottom panel, Nb<sup>5+</sup> peaks are assigned) and H<sub>x</sub>CBNO (top panel, additional Nb<sup>4+</sup> peaks are assigned) samples. (c) UV-vis-NIR transmission spectra of CBNO (cyan line) and H<sub>x</sub>CBNO (orange line) samples. Inset shows ( $\alpha h\nu$ )<sup>2</sup> as a function of incident photon energy  $h\nu$  for the CBNO sample. (d) Temperature-dependent conductance of CBNO (cyan half-filled square) and H<sub>x</sub>CBNO (orange half-filled circle) flakes (with a device channel of about 500  $\mu$ m). Gray lines are linear fittings for the high-temperature regions. Inset shows measured currents under a bias of 10 V for CBNO (cyan line) and H<sub>x</sub>CBNO (orange line) samples as a function of time at room temperature.

 $\mu$ m and a thickness of 100–600 nm and show different colors, e.g., yellow, blue, and purple, because of optical interference.<sup>2</sup> Pt catalyst was deposited on the surface of exfoliated CBNO flakes to decrease the energy barrier for dissociation of H<sub>2</sub>, thereby promoting hydrogenation.<sup>30</sup> Schematics of hydrogenation and dehydrogenation processes are shown in the middle-left and bottom-left panels of Figure 1a, respectively. After hydrogenation, the shiny and colorful pristine flakes became rather dark, and after dehydrogenation the color is recovered. The interference patterns in the dehydrogenated flakes might be from a wedge-shaped air gap between CBNO flakes and Si substrate induced by the mismatched thermal deformation during heating-cooling. In a control experiment, similar pristine CBNO flakes were annealed in air instead of H<sub>2</sub>/Ar, and no color change was observed (Figure S1). Therefore, the reversible color change during hydrogenationdehydrogenation indicates a major change in the optical absorption of CBNO after hydrogenation to H<sub>x</sub>CBNO.

To understand the impact of hydrogenation on the electronic structures, especially the valence state of Nb in CBNO, we performed X-ray photoelectron spectroscopy (XPS) on both pristine CBNO and H<sub>x</sub>CBNO samples (Figure 1b). The full XPS spectra of both samples are given in Figure S2. In the CBNO sample, Gauss—Lorenz fitting yields a set of peaks (3d<sup>5/2</sup> and 3d<sup>3/2</sup> at around 206.2 and 208.9 eV, respectively), which can be assigned to 3d peaks of Nb<sup>5+</sup>.<sup>31</sup> In

the H<sub>x</sub>CBNO sample, an extra set of peaks occurs at around 203.3 and 206.0 eV for 3d<sup>5/2</sup> and 3d<sup>3/2</sup>, respectively, which can be assigned to 3d peaks of Nb4+.32 To rule out any potential surface effect<sup>33</sup> (Figure S3), the spectra shown in Figure 1b were collected after samples were sputtered using Ar for 120 s. The existence of the Nb<sup>4+</sup> signal after sputtering the sample for 420 s (Figure S3a) suggests to us that the hydrogenation of CBNO is a bulk reaction. On the basis of the XPS result, the atomic ratio of Nb4+/H is estimated to be 1:1. Considering the detailed structural characterizations (XRD and HRTEM, shown in Figure S4-6), there is no obvious change in the crystal structure of CBNO after hydrogenation, although a small change in lattice parameter  $c (\sim 0.02 \text{ Å}) (0.17\%)$  can be resolved. Figure S5 shows that the intensities of some reflections after hydrogenation have changed to some extent. The main contribution from oxygen vacancy may be ruled out because this requires nearly 7% oxygen vacancies to be formed in H<sub>x</sub>CBNO, which can lead to obvious changes in lattice parameter c, for instance, ~2% for many layered oxide perovskite.<sup>34</sup> The reduction of Nb<sup>5+</sup> to Nb<sup>4+</sup> can be mainly attributed to electron doping induced by hydrogen interstitials. By now a 1:1 atomic ratio between H and Nb is achieved. We hereafter focus our attention on such samples, i.e., with x = 1 in

Optical and transport properties of CBNO before and after hydrogenation were studied. Figure 1c shows ultraviolet—

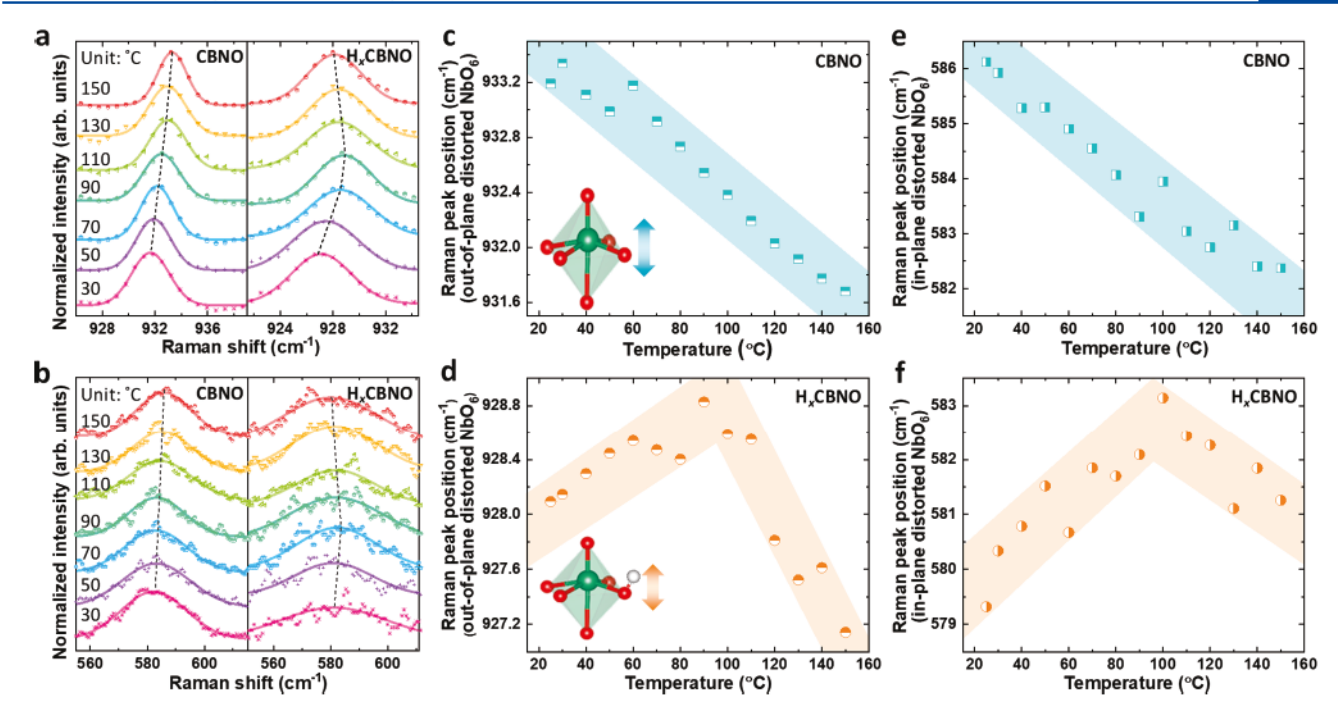


Figure 2. Crystal lattice dynamic of CBNO and  $H_x$ CBNO. (a and b) Temperature-dependent Raman spectra of CBNO (left panels) and  $H_x$ CBNO (right panels) with Raman shift around 930 cm<sup>-1</sup> (a) and 580 cm<sup>-1</sup> (b). The displayed temperature range is from 30 to 150 °C with a step of 20 °C. (c-f) Temperature-dependent Raman peak positions for out-of-plane phonons in CBNO (c) and  $H_x$ CBNO (d) and in-plane phonons of CBNO (e) and  $H_x$ CBNO (f). Insets in panels c and d are sketches of the respective vibration mode in the NbO<sub>6</sub> octahedron. Phonon softening is observed for both out-of-plane and in-plane phonons in  $H_x$ CBNO, indicating that the octahedral distortion can be modified by hydrogenation.

visible—near-infrared (UV—vis—NIR) transmission spectra of both CBNO (cyan curve) and  $H_x$ CBNO (orange curve) samples. The absorption coefficient ( $\alpha$ ) of  $H_x$ CBNO (more than 60%) is at least five times greater than that of CBNO (about 10%) in the 400 to 2500 nm range. By plotting  $(\alpha h\nu)^2$  as a function of incident photon energy  $h\nu$ , 35 as shown in the inset of Figure 1c, a direct band gap of 3.6 eV for CBNO can be identified (greater than a computational value of 2.7 eV<sup>36</sup>). Absorption cutoff edge for  $H_x$ CBNO, though vague, should be at a much lower value than CBNO as analyzed in Figure S7.

Lateral devices (with size of about 500 (channel length)  $\times$  200 (width)  $\times$  10 (height)  $\mu$ m<sup>3</sup>) were fabricated based on both CBNO and H<sub>x</sub>CBNO flakes to perform temperature-dependent conductance measurements, as shown in Figure 2d. The conductance of a semiconductor with a single source of ionization follows<sup>37</sup>

$$\sigma = A \exp(-E_{\rm a}/k_{\rm B}T) \tag{1}$$

where  $\sigma$  is conductance,  $E_{\rm a}$  activation energy,  $k_{\rm B}$  Boltzmann constant, and A a constant. By linear fitting of conductance curves at high temperature (470–570 K for CBNO and 370–540 K for H<sub>x</sub>CBNO), activation energies of 0.333 and 0.108 eV were obtained for CBNO and H<sub>x</sub>CBNO samples, respectively. Because the ionization energies of both samples are much lower than their optical band gaps, conduction in CBNO and H<sub>x</sub>CBNO within the observed temperature window is dominated by energy levels inside the band gap. Additionally, the conductance of the H<sub>x</sub>CBNO sample at room temperature is about 1 order of magnitude greater than that of the CBNO sample, as indicated in the inset of Figure 1d.

At this stage, although the exact band structure of  $H_x$ CBNO is unknown, spectroscopy, optical, and transport measurements so far indicate that (1) up to 50% of Nb<sup>5+</sup> in  $H_x$ CBNO can be reduced to Nb<sup>4+</sup> by hydrogenation, and (2) unlike the Nb<sup>4+</sup> in

metallic SrNbO $_3$  (4d correlated oxide with  $\delta$  < 0.5%, where  $\delta$  represents the relative percentage of anisotropic distortion in the octahedron NbO $_6$ ; see more information in Figure S8),  $H_x$ CBNO behaves as a semiconductor with a reduced band gap as compared to CBNO. We hypothesize that the unexpected semiconducting behaviors in  $H_x$ CBNO might be related to the extremely high distortion of the NbO $_6$  octahedron ( $\delta$  > 10%) compared to other 4d perovskite oxides (discussed further below).

The crystal lattice dynamics of CBNO and H<sub>x</sub>CBNO samples were investigated by temperature-dependent Raman measurements. Panels a and b of Figure 2 show Raman shifts at around 930 and 580 cm<sup>-1</sup>, respectively. The Raman peak around 930 cm<sup>-1</sup> can be assigned to the out-of-plane vibration mode of NbO<sub>6</sub> (out-of-plane phonon), and the Raman peak around 580 cm<sup>-1</sup> can be assigned to the in-plane vibration mode of NbO<sub>6</sub> (in-plane phonon).<sup>38</sup> The difference between the dynamic behavior of phonon modes belonging to CBNO and H<sub>x</sub>CBNO can be observed, as indicated by dashed curves in Figure 2a,b. The temperature-dependent peak positions of both out-of-plane and in-plane modes in CBNO and H<sub>x</sub>CBNO samples are extracted from Figure 2a,b and plotted in Figure 2c-f. Both modes in CBNO (Figure 2c,e) show decreased frequencies with increasing temperature, which could be due to thermal expansion of the lattice and phonon–phonon interaction.  $^{39-41}$  However, both phonon modes in  $H_xCBNO$ (Figure 2d,f) show remarkably different behavior as compared with those in CBNO, i.e., phonon softening and abnormal shift. The softening of both phonons in H<sub>x</sub>CBNO might indicate a reduced distortion of NbO6 octahedron after hydrogenation,<sup>38</sup> as sketched in the insets of Figure 2c,d. It should be noted that this difference in lattice dynamics may not be easily observed by the XRD or TEM mentioned before. The abnormal increase in frequency of both phonons in

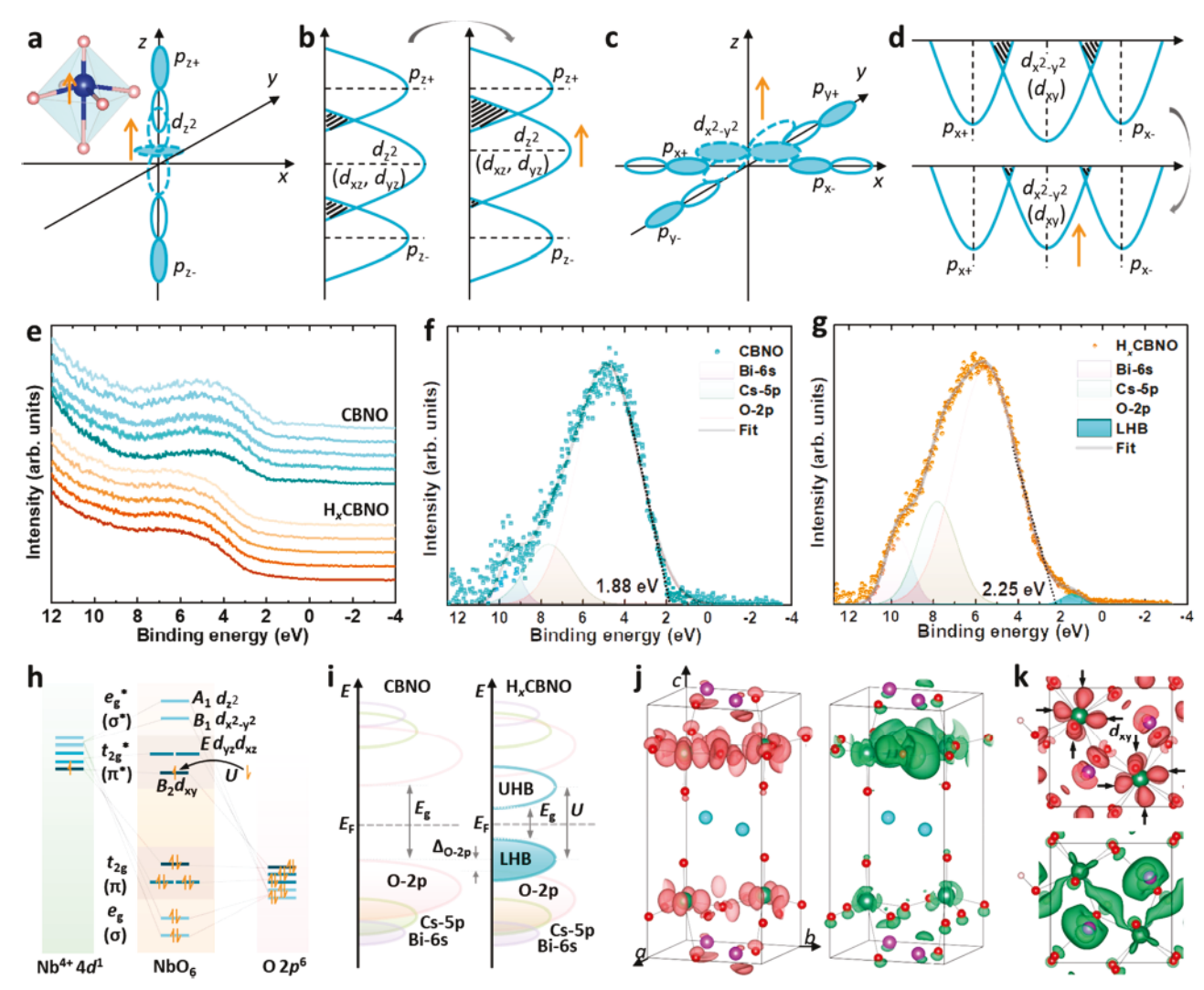


Figure 3. Electronic band reconfiguration of CBNO upon hydrogenation. (a–d) Sketches of bonding (a and c) and cross-sectional overlaps (b and d) between d orbitals and p orbitals ( $d_z^2$  (a);  $d_x^2 - g^2$  (c); and  $p_{x+}$ ,  $p_{y+}$ ,  $p_{x-}$ ,  $p_{y-}$ , and  $p_z$  orbitals) under an off-center distortion. The inset of panel a shows an octahedron under an off-center distortion (indicated by orange arrows). (e) UPS spectra of CBNO (cyan curves) and  $H_x$ CBNO (orange curves). (f and g) Valence band spectra of CBNO (f) and  $H_x$ CBNO (g) after subtracting the background of panel e. The valence band of CBNO is a hybridized one from Bi 6s (Bi6s, purple), Cs 5p (Cs-5p, green), and O 2p (O-2p, pink) orbitals. The additional cyan band in panel g is assigned to an LHB. (h) Molecular orbital diagram of  $H_x$ CBNO. A singly split orbital  $d_{xy}$  with a low energy level is due to off-center octahedral distortion. U is the on-site Coulomb repulsion. (i) Proposed band diagram of CBNO before (left panel) and after hydrogenation (right panel).  $E_g$  is band gap.  $E_F$  is Fermi level.  $\Delta_{O-2p} = 0.37$  eV. (j and k) Charge density redistribution of  $H_x$ CBNO (x = 1): bird's-eye views (j) and top views (k). Pink isosurface represents charge gain, and green isosurface represents charge depletion. The isosurface value is 0.004 e Bohr<sup>-3</sup>. Color code: Cs, cyan; Bi, purple; Nb, green; O, red; H, white. The  $d_{xy}$  orbitals are indicated by black arrows in the top panel of k.

H<sub>x</sub>CBNO with increasing temperature and turning points at around 95 °C may be attributed to a competition between partial dehydrogenation induced by laser heating and phonon softening as a result of increasing temperature.

The high structural distortion in many correlated oxide perovskites can be classified as Jahn–Teller distortion.  $^{42-52}$  Figure S9a shows a typical elongation mode of Jahn–Teller distortion. Though Jahn–Teller distortion stems from crystal field theory, it can be understood by the sketches in Figure S9b–f (for simplicity and purposes of illustration, we use a parabola to represent all orbitals which does not change the conclusion qualitatively). The elongation in the z direction and the compression in both x and y directions result in splitting of energy levels a higher level consisting of  $d_{x^2-y^2}$  orbital and a lower level consisting of a single  $d_{xy}$  orbital and a lower degenerate

level consisting of  $d_{xz}$  and  $d_{yz}$  orbitals from the  $t_{2g}$  set, respectively, as shown in the right panel of Figure S9a. This can be explained by molecular orbital theory based on the increased overlap of  $d_{x^2-y^2}$  (Figure S9b) and  $d_{xy}$  (Figure S9d) orbitals with ligands and the decreased overlap of d<sub>z</sub><sup>2</sup> (Figure S9c), dxz (Figure S9e), and dyz (Figure S9f) orbitals with ligands. In addition to the classical Jahn-Teller type of distortion, off-center distortion (defined as the distortion of an octahedral structure whose inner atom shifts away from its geometric center, a simple model is shown in the inset of Figure 3a) can be found in many Dion-Jacobson layered perovskite oxides. 18,53-55 This off-center distortion reflects an electronic configuration different than that of the classical Jahn-Teller distortion (not including pseudo Jahn-Teller distortion<sup>56</sup>), as demonstrated with sketches in Figures 3a-d and S10. Because of the increased overlap (Figure 3b) of  $d_{z^2}$ 

(Figure 3a),  $d_{xz}$  (Figure S10a), and  $d_{yz}$  (Figure S10b) orbitals with ligands and the decreased overlap (Figure 3d) of  $d_x^2-y^2$  (Figure 3c) and  $d_{xy}$  (Figure S10c) orbitals with ligands, a higher energy level consisting of a  $d_z^2$  orbital and a lower level consisting of a  $d_x^2-y^2$  orbital from the  $e_g$  set and a higher degenerated level consisting of  $d_{xz}$  and  $d_{yz}$  orbitals and a lower single level consisting of a  $d_{xy}$  orbital from the  $t_{2g}$  set may be expected.

The symmetry of the NbO6 octahedron in CBNO can be approximated as  $C_{4\nu}$  (character table is shown in Table S1) because the displacement of Nb from the octahedral center along the c direction  $\delta_c$  (~0.35 Å) is much larger than the displacement along the a (or b) direction  $\delta_a$  (or  $\delta_b$ , ~0.05 Å).<sup>18</sup> Hence, the above molecular orbital analysis can be applied to CBNO and the molecular orbital diagram can be proposed as shown in Figure 3h. Generally among 4d perovskite oxides, without much lattice distortion, if Nb<sup>5+</sup> is reduced into Nb<sup>4+</sup> (having a 4d1 electronic state), a metallic state can be formed, such as in SrNbO<sub>3</sub>. 57-59 However, in a perovskite with a highly distorted octahedron, such as HxCBNO, the lifting of orbital degeneracy may lead to the distorted material being an insulating phase. For instance, according to the Hubbard model, on-site Coulomb repulsion (U in Figure 3h,i) between 4d electrons on a half-filled singly separated  $d_{xy}$  orbital (Figure 3h) can induce an empty upper Hubbard band (UHB) and a fully filled lower Hubbard band (LHB), making the crystal behave like a correlated Mott insulator.1

To verify our hypothesis, we characterized the valence bands of CBNO and H<sub>x</sub>CBNO by ultraviolet photoelectron spectroscopy (UPS). Figure 3e shows the measured spectra for both CBNO and HxCBNO, and detailed analysis is shown in Figure 3f,g. After hydrogenation, an additional narrow band appears near the Femi level (shown as cyan in Figure 3g). From the band shape alone this is consistent with an impurity band or the onset of an LHB, and the case for the Hubbard interpretation is supported by the XPS data in Figure 1b. By linear extrapolations, 60 as shown by dotted lines in Figure 3f,g, the edges of O 2p bands of CBNO and HxCBNO are determined to be 1.88 and 2.25 eV, respectively. This blue shift of O 2p band edge due to hydrogenation ( $\Delta_{O-2p} \approx 0.37 \text{ eV}$ ) indicates a lower degree of orbital splitting (or distortion of NbO<sub>6</sub>) in H<sub>2</sub>CBNO compared with CBNO, consistent with our Raman analysis. Given these UPS analyses, band diagrams of both CBNO and H<sub>x</sub>CBNO are proposed, as shown in Figure 3i. After hydrogenation, the O 2p band shifts down and the LHB is fully filled while the UHB is empty, resulting in a reduced band gap.

The charge density distribution of H<sub>x</sub>CBNO was obtained by first-principles density functional theory (DFT) calculations. After relaxation, the most stable structure is found to be the H atom bonding to the O at the lateral Nb-O layer (Figures 3j,k and S12c,d). Figures 3j,k and S11 show a bird'seye view, a top view, and a side view, respectively, of charge gain (pink isosurface) and charge depletion (green isosurface) in  $H_x$ CBNO (x = 1, two hydrogen atoms in the unit cell with H:Cs = 1:1). Clearly, hydrogen atoms donate their electrons to the crystal and Nb atoms gain electrons. The gained electrons are distributed in the planar dxy orbital, as indicated by black arrows in Figure 3k. A similar charge density redistribution can be found in  $H_x$ CBNO (x = 0.5, one hydrogen atom in a unit cell with H:Cs = 1:2), as shown in Figures S12 and S13. The DFT results are consistent with our analysis based on molecular orbital theory.

The use of strongly correlated materials for artificial intelligence  $^{24,25,61}$  is a burgeoning field; the ultrasensitive nature of correlated materials to external stimuli such as electron doping makes them ideal candidates for highefficiency, fast-response, and multipurpose artificial neural elements.  $^{62-66}$  The observed electronic phase transition and proton-induced plasticity in  $H_x$ CBNO are a great analogy to the synaptic behavior in neuromorphic computing (see more information in Supporting Discussions and Figures S14—S16).

The pronounced doping effect, featuring the reduced band gap and electrical resistance, and the presence of a possible Mott—Hubbard band structure are observed in a quasi-2D niobate crystal. The understanding of the role of hydrogen in 4d transition metal system inspires a new way to design and manipulate the electronic phase of complex materials, which could be potentially useful for future computing.

# METHODS

Molten-Salt Synthesis of CBNO. CsCl (Sigma-Aldrich, 99.9%) was used as the solvent (molten salt). Precursors were  $Cs_2CO_3$  (Sigma-Aldrich, 99%),  $Bi_2O_3$  (Sigma-Aldrich, 99.9%), and  $Nb_2O_5$  (Sigma-Aldrich, 99.9%). The weight ratio of CsCl to all precursors was 10:1 (adjusting this ratio led to CBNO flakes of different sizes). A cooling rate of 0.1 °C/min was used to synthesize centimeter-size CBNO flakes. Detailed growth processes can be found in our previous report.  $^{67}$ 

Hydrogenation of CBNO. The hydrogen spillover method with nanosized Pt catalyst was used for the hydrogenation of CBNO. Pt nanoparticles were deposited on the surface of CBNO flakes by sputtering (Cressington 108auto SEM sputter coater). Then, the samples were annealed for 8 h at 1 atm in Ar/H<sub>2</sub> (5% H<sub>2</sub>) gas at 475 °C. No obvious change was observed for samples annealed at temperatures below 425 °C, while samples decomposed at temperatures above 500 °C. After annealing, the samples were cooled to room temperature at a cooling rate of 5 °C/min and with an Ar/H<sub>2</sub> gas flow. Dehydrogenation was achieved by annealing in air (350 °C for 30 min, for example).

Structural Characterization of CBNO and H<sub>x</sub>CBNO. The morphology of CBNO and H<sub>r</sub>CBNO flakes was characterized by a Nikon Eclipse Ti-S inverted optical microscope. X-ray diffraction (XRD) tests were conducted on a Panalytical X'Pert PRO MPD system with a Bruker D8 Discover X-ray diffractometer (Cu K $\alpha$ ,  $\lambda$  = 1.5405 Å) and a point detector.  $\omega$ -2 $\theta$  spectra were acquired with a divergent beam Bragg-Brentano geometry over a large  $2\theta$  range from  $5^{\circ}$  to  $80^{\circ}$  to detect small inclusions of possible secondary phases or misoriented grains. Transmission electron microscopy (TEM) (JEOL JEM-2010) was used to collect the structural information on both CBNO and HxCBNO flakes, including high-resolution TEM images (HRTEM) and electron diffraction patterns. Raman spectra were collected using a WITec Alpha 300 confocal Raman microscope with an excitation source of 532 nm in air.

Transport, Optical, Valence State, and Valence Band Measurements. Transport measurements were performed on lateral-contact devices. Flakes were transferred to a sapphire substrate (MTI Corporation), and two electrodes were made using conductive silver paint (Ted Pella, Inc.). Currents as a function of time (I-t) were measured before and after hydrogenation with an Autolab PGSTAT302N potentiostat. In temperature-dependent conductance  $(\sigma-T)$  measurements, samples were placed on top of a thermal stage. Liquid nitrogen was used to

ensure a temperature ramping rate of less than 5 °C/min and to keep the temperature stable during measurements. Measurements were conducted in nitrogen gas to prevent oxidations. The thermal stage, temperature controller, and liquid nitrogen pump were all from Linkam. The transmission spectra were measured via a PerkinElmer Lambda 950 UV—vis—NIR spectrophotometer with a Photomultiplier R6872 detector. X-ray photoelectron spectroscopy and ultraviolet photoelectron spectroscopy tests were conducted using a PHI 5000 VersaProbe System. Ar ion sputter was used to clean the surface of samples before measuring. UPS data were recorded with a multichannel electrostatic hemispherical electronic analyzer. Al  $K\alpha$  (1486.6 eV) was used for core-level spectroscopy, while He I $\alpha$  (21.22 eV) radiation from a high-flux discharge lamp was used for valence-band spectroscopy.

DFT Calculation. The DFT calculations were performed with the Vienna Ab Initio Simulation Package (VASP 5.4.4).68 The Perdew-Burke-Ernzerhof (PBE)<sup>69</sup> exchange-correlation function was used. The projector augmented wave method<sup>70</sup> was employed. An optimization about the position of the H atom in the unit cell has been conducted. For the full structure relaxation, a  $\Gamma$ -centered k-point mesh of  $4 \times 4 \times 2$  was applied to sample the Brillouin zone, and Gaussian smearing with  $\sigma$  of 0.1 eV was used. The kinetic energy cutoff for plane wave basis was set to 500 eV. The energy difference for electronic convergence criterion was set to less than  $1 \times 10^{-5}$  eV, and ionic relaxation force was less than 0.01 eV/Å on each atom. Spin-orbit coupling (SOC) was included in geometry optimization and electronic structure calculations. The charge density difference was obtained by subtracting the charge density of pure CBNO and isolated H atoms from the charge density of H<sub>x</sub>CBNO.

Neural Network Simulations. CrossSim was used for simulation.<sup>71</sup> The simulation was based on a supervised learning algorithm with backpropagation and "sigmoid" nonlinear activation function. 71-73 In the simulation, H<sub>x</sub>CBNO-based proton synaptic transistors were used in a crossbar to perform two matrix operations. The numerical weights in the network layer were mapped onto the device conductance states, and the mapping was designed so that most of the weights stay in 25%-75% of the conductance range to minimize the impact of nonlinearity. Two standard data sets (an 8 × 8-pixel image version of handwritten digits) from University of California at Irvine (UCI) image data set and a 28  $\times$  28 pixel image version of handwritten digits<sup>75</sup> from the Modified National Institute of Standards and Technology (MNIST) image data set) were used for classification and training. To update a weight, the initial conductance,  $G_0$ , of the device was first determined; the state was then updated by the average change of conductance ( $\Delta G$ ).  $\Delta G$  was scaled based on the updated size calculated by the backpropagation algorithm. The detailed simulation process can be found in ref 76.

## ASSOCIATED CONTENT

## Supporting Information

The Supporting Information is available free of charge at https://pubs.acs.org/doi/10.1021/acs.jpclett.1c00353.

Optical properties, elemental analysis, structural analysis, orbital splitting due to distortions, DFT calculation of charge density redistribution after hydrogenation, neural network simulations, character table for group  $C_{4\nu}$  and data sets used for neuromorphic simulation (PDF)

## AUTHOR INFORMATION

## **Corresponding Author**

Jian Shi — Department of Materials Science and Engineering, Rensselaer Polytechnic Institute, Troy, New York 12180, United States; orcid.org/0000-0003-2115-2225; Email: shij4@rpi.edu

#### Authors

- Lifu Zhang Department of Materials Science and Engineering, Rensselaer Polytechnic Institute, Troy, New York 12180, United States
- Jie Jiang Department of Materials Science and Engineering, Rensselaer Polytechnic Institute, Troy, New York 12180, United States
- Yao Cai The Institute of Technological Sciences, Wuhan University, Wuhan 430072, PR China
- Shukai Yao School of Materials Engineering, Purdue University, West Lafayette, Indiana 47907, United States
- Bilal Azhar Department of Materials Science and Engineering, Cornell University, Ithaca, New York 14850, United States
- Zhizhong Chen Department of Materials Science and Engineering, Rensselaer Polytechnic Institute, Troy, New York 12180, United States
- Yang Hu Department of Materials Science and Engineering, Rensselaer Polytechnic Institute, Troy, New York 12180, United States
- Saloni Pendse Department of Materials Science and Engineering, Rensselaer Polytechnic Institute, Troy, New York 12180, United States
- Yuwei Guo Department of Materials Science and Engineering, Rensselaer Polytechnic Institute, Troy, New York 12180, United States
- Ru Jia Department of Materials Science and Engineering, Rensselaer Polytechnic Institute, Troy, New York 12180, United States
- Zhiting Tian Sibley School of Mechanical and Aerospace Engineering, Cornell University, Ithaca, New York 14850, United States
- Chengliang Sun The Institute of Technological Sciences, Wuhan University, Wuhan 430072, PR China; orcid.org/ 0000-0003-1986-2674
- Peilin Liao School of Materials Engineering, Purdue University, West Lafayette, Indiana 47907, United States

Complete contact information is available at: https://pubs.acs.org/10.1021/acs.jpclett.1c00353

# **Author Contributions**

T.Z. and J.J. contributed equally to this work.

### Notes

The authors declare no competing financial interest.

# ACKNOWLEDGMENTS

The computational research was supported in part through computational resources provided by the Information Technology department at Purdue University, West Lafayette, Indiana. Y.G. and J.S. acknowledge the Air Force Office of Scientific Research under Award Number FA9550-18-1-0116. L.Z. acknowledges the New York State's Empire State Development's Division of Science, Technology and Innovation through Focus Center Contract C150117. Z.C. and Y.H. acknowledge support from the US National Science

Foundation under Award Numbers 1706815 and 1916652. This material is partially based on work supported by the NSF-MIP Platform for the Accelerated Realization, Analysis, and Discovery of Interface Materials (PARADIM) under cooperative Agreement No. DMR1539918. This work made use of the Cornell Center for Materials Research Facilities supported by the National Science Foundation under Award Number DMR-1719875.

# REFERENCES

- (1) Imada, M.; Fujimori, A.; Tokura, Y. Metal-insulator transitions. Rev. Mod. Phys. 1998, 70, 1039–1263.
- (2) Yang, Z.; Ko, C.; Ramanathan, S. Oxide Electronics Utilizing Ultrafast Metal-Insulator Transitions. *Annu. Rev. Mater. Res.* 2011, 41, 337–367.
- (3) Kumar, S.; Strachan, J. P.; Williams, R. S. Chaotic dynamics in nanoscale  $NbO_2$  Mott memristors for analogue computing. *Nature* 2017, 548, 318.
- (4) Dagotto, E. Complexity in Strongly Correlated Electronic Systems. *Science* 2005, 309, 257–262.
- (5) del Valle, J.; Salev, P.; Tesler, F.; Vargas, N. M.; Kalcheim, Y.; Wang, P.; Trastoy, J.; Lee, M.-H.; Kassabian, G.; Ramírez, J. G.; et al. Subthreshold firing in Mott nanodevices. *Nature* 2019, 569, 388–392.
- (6) Zhou, Y.; Ramanathan, S. Mott Memory and Neuromorphic Devices. *Proc. IEEE* 2015, 103, 1289-1310.
- (7) Pickett, M. D.; Medeiros-Ribeiro, G.; Williams, R. S. A scalable neuristor built with Mott memristors. *Nat. Mater.* 2013, *12*, 114–117.
- (8) Stoliar, P.; Tranchant, J.; Corraze, B.; Janod, E.; Besland, M.-P.; Tesler, F.; Rozenberg, M.; Cario, L. A Leaky-Integrate-and-Fire Neuron Analog Realized with a Mott Insulator. *Adv. Funct. Mater.* 2017, 27, 1604740.
- (9) von Helmolt, R.; Wecker, J.; Holzapfel, B.; Schultz, L.; Samwer, K. Giant negative magnetoresistance in perovskitelike La<sub>2/3</sub>Ba<sub>1/3</sub>MnO<sub>x</sub> ferromagnetic films. *Phys. Rev. Lett.* 1993, 71, 2331–2333.
- (10) Jaramillo, R.; Ha, S. D.; Silevitch, D.; Ramanathan, S. Origins of bad-metal conductivity and the insulator—metal transition in the rareearth nickelates. *Nat. Phys.* 2014, *10*, 304.
- (11) Lu, N.; Zhang, P.; Zhang, Q.; Qiao, R.; He, Q.; Li, H.-B.; Wang, Y.; Guo, J.; Zhang, D.; Duan, Z.; et al. Electric-field control of tri-state phase transformation with a selective dual-ion switch. *Nature* 2017, 546, 124–128.
- (12) Chen, S.; Zhou, H.; Ye, X.; Chen, Z.; Zhao, J.; Das, S.; Klewe, C.; Zhang, L.; Lupi, E.; Shafer, P.; et al. Versatile and Highly Efficient Controls of Reversible Topotactic Metal—Insulator Transitions through Proton Intercalation. *Adv. Funct. Mater.* 2019, 29, 1907072.
- (13) Shi, J.; Zhou, Y.; Ramanathan, S. Colossal resistance switching and band gap modulation in a perovskite nickelate by electron doping. *Nat. Commun.* 2014, 5, 4860.
- (14) Chen, J.; Mao, W.; Ge, B.; Wang, J.; Ke, X.; Wang, V.; Wang, Y.; Döbeli, M.; Geng, W.; Matsuzaki, H. Revealing the role of lattice distortions in the hydrogen-induced metal-insulator transition of SmNiO<sub>3</sub>. *Nat. Commun.* 2019, 10, 694.
- (15) Bednorz, J. G.; Müller, K. A. Perovskite-type oxides The new approach to high- $T_c$  superconductivity. *Rev. Mod. Phys.* 1988, 60, 585–600.
- (16) Millis, A. J. Lattice effects in magnetoresistive manganese perovskites. *Nature* 1998, 392, 147–150.
- (17) Wang, K.; Liu, J.-M.; Ren, Z. Multiferroicity: the coupling between magnetic and polarization orders. *Adv. Phys.* 2009, *58*, 321–448.
- (18) Snedden, A.; Knight, K. S.; Lightfoot, P. Structural distortions in the layered perovskites  $CsANb_2O_7$  (A= Nd, Bi). *J. Solid State Chem.* 2003, 173, 309–313.
- (19) Chen, S.; Wang, Z.; Ren, H.; Chen, Y.; Yan, W.; Wang, C.; Li, B.; Jiang, J.; Zou, C. Gate-controlled VO<sub>2</sub> phase transition for high-performance smart windows. *Science Advances* 2019, 5, eaav6815.

- (20) Wei, J.; Ji, H.; Guo, W.; Nevidomskyy, A. H.; Natelson, D. Hydrogen stabilization of metallic vanadium dioxide in single-crystal nanobeams. *Nat. Nanotechnol.* 2012, 7, 357.
- (21) Filinchuk, Y.; Tumanov, N. A.; Ban, V.; Ji, H.; Wei, J.; Swift, M. W.; Nevidomskyy, A. H.; Natelson, D. In situ diffraction study of catalytic hydrogenation of VO<sub>2</sub>: Stable phases and origins of metallicity. *J. Am. Chem. Soc.* 2014, *136*, 8100–8109.
- (22) Yoon, H.; Choi, M.; Lim, T.-W.; Kwon, H.; Ihm, K.; Kim, J. K.; Choi, S.-Y.; Son, J. Reversible phase modulation and hydrogen storage in multivalent VO<sub>2</sub> epitaxial thin films. *Nat. Mater.* 2016, *15*, 1113.
- (23) Shi, J.; Ha, S. D.; Zhou, Y.; Schoofs, F.; Ramanathan, S. A correlated nickelate synaptic transistor. *Nat. Commun.* 2013, 4, 2676.
- (24) Zuo, F.; Panda, P.; Kotiuga, M.; Li, J.; Kang, M.; Mazzoli, C.; Zhou, H.; Barbour, A.; Wilkins, S.; Narayanan, B.; et al. Habituation based synaptic plasticity and organismic learning in a quantum perovskite. *Nat. Commun.* 2017, 8, 240.
- (25) Zhang, H.-T.; Park, T. J.; Zaluzhnyy, I. A.; Wang, Q.; Wadekar, S. N.; Manna, S.; Andrawis, R.; Sprau, P. O.; Sun, Y.; Zhang, Z.; et al. Perovskite neural trees. *Nat. Commun.* 2020, 11, 2245.
- (26) Takabatake, T.; Ye, W.; Orimo, S.; Tamegai, T.; Fujii, H. Hydrogen intercalation in some superconducting copper oxides. *Phys.* C 1989, 162–164, 65–66.
- (27) Celani, F.; Boutet, M.; di Gioacchino, D.; Spallone, A.; Tripodi, P.; Pace, S.; Polichetti, M.; Marini, P. First results about hydrogen loading by means of pulsed electrolysis of Y<sub>1</sub>Ba<sub>2</sub>Cu<sub>3</sub>O<sub>7</sub> pellets. *Phys. Lett. A* 1994, 189, 395–402.
- (28) Kulischow, N.; Ladasiu, C.; Marschall, R. Layered Dion-Jacobson type niobium oxides for photocatalytic hydrogen production prepared via molten salt synthesis. *Catal. Today* 2017, 287, 65–69.
- (29) Kim, H.-J.; Osada, M.; Ebina, Y.; Sugimoto, W.; Tsukagoshi, K.; Sasaki, T. Hunting for Monolayer Oxide Nanosheets and Their Architectures. Sci. Rep. 2016, 6, 19402.
- (30) Panayotov, D. A.; Yates, J. T. Spectroscopic detection of hydrogen atom spillover from Au nanoparticles supported on TiO<sub>2</sub>: use of conduction band electrons. *J. Phys. Chem. C* 2007, 111, 2959–2964.
- (31) Chastain, J. Handbook of X-ray photoelectron spectroscopy. Perkin-Elmer Corporation 1992, 40, 221.
- (32) Darlinski, A.; Halbritter, J. Angle-resolved XPS studies of oxides at NbN, NbC, and Nb surfaces. Surf. Interface Anal. 1987, 10, 223–237
- (33) Dupin, J.-C.; Gonbeau, D.; Vinatier, P.; Levasseur, A. Systematic XPS studies of metal oxides, hydroxides and peroxides. *Phys. Chem. Phys.* 2000, 2, 1319–1324.
- (34) Nakamura, T.; Ling, Y.; Amezawa, K. The effect of interstitial oxygen formation on the crystal lattice deformation in layered perovskite oxides for electrochemical devices. *J. Mater. Chem. A* 2015, 3, 10471–10479.
- (35) Wood, D. L.; Tauc, J. Weak Absorption Tails in Amorphous Semiconductors. *Phys. Rev. B* 1972, 5, 3144–3151.
- (36) Autieri, C.; Barone, P.; Sławińska, J.; Picozzi, S. Persistent spin helix in Rashba-Dresselhaus ferroelectric CsBiNb<sub>2</sub>O<sub>7</sub>. *Physical Review Materials* 2019, 3, 084416.
- (37) Kasap, S. O. Principles of Electronic Materials and Devices; McGraw-Hill: New York, 2006; Vol. 2.
- (38) Jehng, J. M.; Wachs, I. E. Structural chemistry and Raman spectra of niobium oxides. *Chem. Mater.* 1991, 3, 100–107.
- (39) Link, A.; Bitzer, K.; Limmer, W.; Sauer, R.; Kirchner, C.; Schwegler, V.; Kamp, M.; Ebling, D.; Benz, K. Temperature dependence of the  $E_2$  and  $A_1$  (LO) phonons in GaN and AlN. *J. Appl. Phys.* 1999, 86, 6256–6260.
- (40) Menéndez, J.; Cardona, M. Temperature dependence of the first-order Raman scattering by phonons in Si, Ge, and α-Sn: Anharmonic effects. *Phys. Rev. B: Condens. Matter Mater. Phys.* 1984, 29, 2051.
- (41) Irmer, G.; Wenzel, M.; Monecke, J. The temperature dependence of the LO (T) and TO (T) phonons in GaAs and InP. *Phys. Status Solidi B* 1996, 195, 85–95.

- (42) MacLean, D. A.; Ng, H.-N.; Greedan, J. E. Crystal structures and crystal chemistry of the RETiO<sub>3</sub> perovskites: RE = La, Nd, Sm, Gd, Y. J. Solid State Chem. 1979, 30, 35–44.
- (43) Rodríguez-Carvajal, J.; Hennion, M.; Moussa, F.; Moudden, A. H.; Pinsard, L.; Revcolevschi, A. Neutron-diffraction study of the Jahn-Teller transition in stoichiometric LaMnO<sub>3</sub>. *Phys. Rev. B: Condens. Matter Mater. Phys.* 1998, 57, R3189–R3192.
- (44) Knafo, W.; Meingast, C.; Boris, A. V.; Popovich, P.; Kovaleva, N. N.; Yordanov, P.; Maljuk, A.; Kremer, R. K.; Löhneysen, H. v.; Keimer, B. Ferromagnetism and lattice distortions in the perovskite YTiO<sub>3</sub>. *Phys. Rev. B: Condens. Matter Mater. Phys.* 2009, 79, 054431.
- (45) Yang, J. Structural analysis of perovskite LaCr<sub>1-x</sub>Ni<sub>x</sub>O<sub>3</sub> by Rietveld refinement of X-ray powder diffraction data. *Acta Crystallogr.*, Sect. B: Struct. Sci. 2008, 64, 281–286.
- (46) Dimitrovska-Lazova, S.; Kovacheva, D.; Aleksovska, S.; Marinšek, M.; Tzvetkov, P. Synthesis and structural details of perovskites within the series  $PrCo_{1-x}Cr_xO_3$  (x= 0, 0.33, 0.5, 0.67 and 1). Bulgarian Chem. Commun. 2012, 44, 37–46.
- (47) Maris, G.; Ren, Y.; Volotchaev, V.; Zobel, C.; Lorenz, T.; Palstra, T. T. M. Evidence for orbital ordering in LaCoO<sub>3</sub>. *Phys. Rev. B: Condens. Matter Mater. Phys.* 2003, 67, 224423.
- (48) Bringley, J. F.; Scott, B. A.; La Placa, S. J.; McGuire, T. R.; Mehran, F.; McElfresh, M. W.; Cox, D. E. Structure and properties of the LaCuO<sub>3- $\delta$ </sub> perovskites. *Phys. Rev. B: Condens. Matter Mater. Phys.* 1993, 47, 15269–15275.
- (49) Huang, Q.; Soubeyroux, J. L.; Chmaissem, O.; Sora, I. N.; Santoro, A.; Cava, R. J.; Krajewski, J. J.; Peck, W. F. Neutron Powder Diffraction Study of the Crystal Structures of Sr<sub>2</sub>RuO<sub>4</sub> and Sr<sub>2</sub>IrO<sub>4</sub> at Room Temperature and at 10 K. J. Solid State Chem. 1994, 112, 355—361.
- (50) Shaked, H.; Jorgensen, J. D.; Chmaissem, O.; Ikeda, S.; Maeno, Y. Neutron Diffraction Study of the Structural Distortions in Sr<sub>3</sub>Ru<sub>2</sub>O<sub>7</sub>. *J. Solid State Chem.* 2000, 154, 361–367.
- (51) Goodenough, J. B.; Loeb, A. L. Theory of Ionic Ordering, Crystal Distortion, and Magnetic Exchange Due to Covalent Forces in Spinels. *Phys. Rev.* 1955, *98*, 391–408.
- (52) Dunitz, J. D.; Orgel, L. E. Electronic properties of transition-metal oxides—I: Distortions from cubic symmetry. *J. Phys. Chem. Solids* 1957, 3, 20–29.
- (53) Zhu, T.; Cohen, T.; Gibbs, A. S.; Zhang, W.; Halasyamani, P. S.; Hayward, M. A.; Benedek, N. A. Theory and Neutrons Combine To Reveal a Family of Layered Perovskites without Inversion Symmetry. *Chem. Mater.* 2017, 29, 9489–9497.
- (54) Li, B.-W.; Osada, M.; Ozawa, T. C.; Sasaki, T. RbBiNb<sub>2</sub>O<sub>7</sub>: A New Lead-Free High-*T*<sub>c</sub> Ferroelectric. *Chem. Mater.* 2012, 24, 3111–3113.
- (55) Gopalakrishnan, J.; Bhat, V.; Raveau, B. A<sup>I</sup>LaNb<sub>2</sub>O<sub>7</sub>: A new series of layered perovskites exhibiting ion exchange and intercalation behaviour. *Mater. Res. Bull.* 1987, 22, 413–417.
- (56) Bersuker, I. B. Pseudo-Jahn-Teller Effect—A Two-State Paradigm in Formation, Deformation, and Transformation of Molecular Systems and Solids. *Chem. Rev.* 2013, 113, 1351–1390.
- (57) Turzhevsky, S.; Novikov, D.; Gubanov, V.; Freeman, A. J. Electronic structure and crystal chemistry of niobium oxide phases. *Phys. Rev. B: Condens. Matter Mater. Phys.* 1994, 50, 3200.
- (58) Isawa, K.; Itti, R.; Sugiyama, J.; Koshizuka, N.; Yamauchi, H. Photoelectron spectroscopic study of Sr<sub>x</sub>NbO<sub>3</sub>. *Phys. Rev. B: Condens. Matter Mater. Phys.* 1994, 49, 3534.
- (59) Chen, C.; Lv, S.; Wang, Z.; Akagi, K.; Lichtenberg, F.; Ikuhara, Y.; Bednorz, J. G. Atomic and electronic structure of the SrNbO<sub>3</sub>/SrNbO<sub>34</sub> interface. *Appl. Phys. Lett.* 2014, *105*, 221602.
- (60) Chambers, S. A.; Droubay, T.; Kaspar, T. C.; Gutowski, M. Experimental determination of valence band maxima for SrTiO<sub>3</sub>, TiO<sub>2</sub>, and SrO and the associated valence band offsets with Si(001). *J. Vac. Sci. Technol., B: Microelectron. Process. Phenom.* 2004, 22, 2205–2215.
- (61) Shi, J.; Ha, S. D.; Zhou, Y.; Schoofs, F.; Ramanathan, S. A correlated nickelate synaptic transistor. *Nat. Commun.* 2013, 4, 2676.

- (62) Kumar, S.; Strachan, J. P.; Williams, R. S. Chaotic dynamics in nanoscale  $NbO_2$  Mott memristors for analogue computing. *Nature* 2017, 548, 318–321.
- (63) Kumar, S.; Wang, Z.; Davila, N.; Kumari, N.; Norris, K. J.; Huang, X.; Strachan, J. P.; Vine, D.; Kilcoyne, A. L. D.; Nishi, Y.; et al. Physical origins of current and temperature controlled negative differential resistances in NbO<sub>2</sub>. *Nat. Commun.* 2017, *8*, 658.
- (64) Wang, Z.; Joshi, S.; Savel'ev, S. E.; Jiang, H.; Midya, R.; Lin, P.; Hu, M.; Ge, N.; Strachan, J. P.; Li, Z.; et al. Memristors with diffusive dynamics as synaptic emulators for neuromorphic computing. *Nat. Mater.* 2017, *16*, 101–108.
- (65) Wang, Z.; Rao, M.; Han, J.-W.; Zhang, J.; Lin, P.; Li, Y.; Li, C.; Song, W.; Asapu, S.; Midya, R.; et al. Capacitive neural network with neuro-transistors. *Nat. Commun.* 2018, 9, 3208.
- (66) Li, C.; Wang, Z.; Rao, M.; Belkin, D.; Song, W.; Jiang, H.; Yan, P.; Li, Y.; Lin, P.; Hu, M.; et al. Long short-term memory networks in memristor crossbar arrays. *Nature Machine Intelligence* 2019, 1, 49–57.
- (67) Pendse, S.; Jiang, J.; Guo, Y.; Zhang, L.; Chen, Z.; Lu, Z.; Wang, Y.; Hu, Y.; Li, S.; Feng, J.; et al. Unit-Cell-Thick Oxide Synthesis by Film-Based Scavenging. *J. Phys. Chem. C* 2020, 124, 8394–8400.
- (68) Kresse, G.; Furthmüller, J. Efficient iterative schemes for ab initio total-energy calculations using a plane-wave basis set. *Phys. Rev. B: Condens. Matter Mater. Phys.* 1996, 54, 11169–11186.
- (69) Perdew, J. P.; Burke, K.; Ernzerhof, M. Generalized Gradient Approximation Made Simple. *Phys. Rev. Lett.* 1996, 77, 3865–3868.
- (70) Kresse, G.; Joubert, D. From ultrasoft pseudopotentials to the projector augmented-wave method. *Phys. Rev. B: Condens. Matter Mater. Phys.* 1999, 59, 1758–1775.
- (71) Agarwal, S.; Plimpton, S. J.; Hughart, D. R.; Hsia, A. H.; Richter, I.; Cox, J. A.; James, C. D.; Marinella, M. J. Resistive memory device requirements for a neural algorithm accelerator. 2016 International Joint Conference on Neural Networks (IJCNN); IEEE, 2016; pp 929–938.
- (72) Fuller, E. J.; Gabaly, F. E.; Léonard, F.; Agarwal, S.; Plimpton, S. J.; Jacobs-Gedrim, R. B.; James, C. D.; Marinella, M. J.; Talin, A. A. Li-ion synaptic transistor for low power analog computing. *Adv. Mater.* 2017, 29, 1604310.
- (73) van de Burgt, Y.; Lubberman, E.; Fuller, E. J.; Keene, S. T.; Faria, G. C.; Agarwal, S.; Marinella, M. J.; Talin, A. A.; Salleo, A. A non-volatile organic electrochemical device as a low-voltage artificial synapse for neuromorphic computing. *Nat. Mater.* 2017, *16*, 414–418.
- (74) Bache, K.; Lichman, M. UCI machine learning repository. University of California at Irvine: School of Information and Computer Science: Irvine, CA, 2016.
- (75) Lecun, Y.; Bottou, L.; Bengio, Y.; Haffner, P. Gradient-based learning applied to document recognition. *Proc. IEEE* 1998, 86, 2278-2324.
- (76) Fuller, E. J.; Gabaly, F. E.; Léonard, F.; Agarwal, S.; Plimpton, S. J.; Jacobs-Gedrim, R. B.; James, C. D.; Marinella, M. J.; Talin, A. A. Li-Ion Synaptic Transistor for Low Power Analog Computing. *Adv. Mater.* 2017, 29, 1604310.